The Astrophysical Journal, 788:188 (13pp), 2014 June 20 doi:10.1088/0004-637X/788/2/188

FAINT DWARFS IN NEARBY GROUPS

Ryan Speller and James E. Taylor
Department of Physics and Astronomy, University of Waterloo, Waterloo, ON N2L 3G1, Canada; rspeller@uwaterloo.ca, taylor@uwaterloo.ca
Received 2013 March 27; accepted 2014 May 4; published 2014 June 6

ABSTRACT

The number and distribution of dwarf satellite galaxies remain a critical test of cold dark matter–dominated structure formation on small scales. Until recently, observational information about galaxy formation on these scales has been limited mainly to the Local Group. We have searched for faint analogues of Local Group dwarfs around nearby bright galaxies, using a spatial clustering analysis of the photometric catalog of the Sloan Digital Sky Survey (SDSS) Data Release 8. Several other recent searches of SDSS have detected clustered satellite populations down to $\Delta m_r \equiv (m_{r,\,\mathrm{sat}} - m_{r,\,\mathrm{main}}) \sim 6$–8, using photometric redshifts to reduce background contamination. SDSS photometric redshifts are relatively imprecise, however, for faint and nearby galaxies. Instead, we use angular size to select potential nearby dwarfs and consider only the nearest isolated bright galaxies as primaries. As a result, we are able to detect an excess clustering signal from companions down to $\Delta m_r = 12$, 4 mag fainter than most recent studies. We detect an overdensity of objects at separations <400 kpc, corresponding to about 4.6 ± 0.5 satellites per central galaxy, consistent with the satellite abundance expected from the Local Group, given our selection function. Although the sample of satellites detected is incomplete by construction, since it excludes the least and most compact dwarfs, this detection provides a lower bound on the average satellite luminosity function, down to luminosities corresponding to the faintest "classical" dwarfs of the Local Group.

Key words: dark matter – galaxies: dwarf – galaxies: formation – galaxies: groups: general – galaxies: luminosity function, mass function – Local Group

Online-only material: color figures

1. INTRODUCTION

One of the great challenges of cosmology is to explain the range of galaxy properties observed in the present-day universe. Galaxy formation has long been expected to have natural cutoffs on large and small scales, as gas cooling becomes inefficient at the high/low virial temperatures expected in massive/low-mass structures. This argument provided the original framework for understanding why individual galaxies have the range of masses and sizes they do, with fairly well defined upper and lower limits (Silk 1977; Rees & Ostriker 1977; White & Rees 1978). The subsequent development of cosmological models dominated by cold dark matter (CDM) made the argument more precise; the basic framework for CDM galaxy formation, as outlined in White & Frenk (1991), combines hierarchical structure formation in the dark sector with the physics of gas cooling and star formation in the baryonic sector. In the two decades since this picture was introduced, however, it has become increasingly clear that the mass function of dark matter halos predicted by CDM models is very different from the luminosity function of galaxies observed in the field (e.g., Kauffmann et al. 1993; Klypin et al. 1999; Moore et al. 1999; Benson et al. 2003; Behroozi et al. 2013). In particular, if the universe is full of the small-scale structure predicted by CDM models, most of this structure must remain unilluminated by stars.

While the existence of a lower cutoff scale for galaxy formation is clear, the detailed nature of the cutoff is much less so. In principle, the cutoff scale could be sharp and well-defined, such that all halos above some mass and none of the halos below that mass are occupied by galaxies. Alternately, it could be that star formation gradually dies out over a broad range of halo mass. In the latter case, we can think of galaxy formation on small scales as being *stochastic*, either in the sense that it is truly random, or in the sense that that it is determined by one or more "hidden" variables other than halo mass. There are several plausible candidates for hidden variables controlling galaxy formation, including merger history, age, environment, and/or star-formation history.

The least massive galaxies we know of are dwarf satellites of the Milky Way (MW) or the Andromeda galaxy (M31), located within a few hundred kiloparsecs of us. In the CDM model they should correspond to subhalos within the larger dark matter halos of the two main galaxies of the Local Group. The correspondence between galaxies and CDM structure is particularly puzzling on these scales, however. The velocity dispersions of the Local Group satellites suggest that at least some of them may occupy relatively low-mass subhalos, but simulations predict many more subhalos on these scales than there are known satellites (Moore et al. 1999; Klypin et al. 1999). Is this an indication of stochasticity in dwarf galaxy formation? If all the CDM structure predicted by simulations is truly present in the halo of the MW, what sets apart the few subhalos where dwarf satellites have formed? The paucity of observed dwarf satellites has been called the "missing satellite" problem, but in a sense it is the opposite. Given the many mechanisms at work to suppress galaxy formation on small scales—supernova feedback (Dekel & Silk 1986; Mashchenko et al. 2008; Governato et al. 2010), reionization (Efstathiou 1992; Barkana & Loeb 1999; Bullock et al. 2000; Gnedin & Kravtsov 2006), "harassment" (Moore et al. 1996), ram-pressure stripping (Gunn & Gott 1972; Nichols & Bland-Hawthorn 2011) and/or tidal forces (Taylor & Babul 2001; Mayer et al. 2006; Łokas et al. 2012)—the real question is perhaps, why do we see any dwarf satellites at all?

A major obstacle to resolving the missing satellite problem conclusively is the absence of data for a greater number of groups. Our only reasonably complete samples of brighter satellites are around the two main galaxies of the Local Group, or a handful of other nearby systems (Karachentsev 2005). In

the case of the extremely low surface-brightness "ultra-faint" dwarfs with $M_V \lesssim -8$ (Willman et al. 2005; Belokurov et al. 2006; Zucker et al. 2006), only the MW's population is known, and even it is likely to be significantly incomplete (Koposov et al. 2008; Tollerud et al. 2008). This raises the question of how representative the MW or Local Group satellite populations are.

In particular, there has been much recent discussion of the relative frequency of bright satellites such as the LMC, SMC, M33, or M32, and what this implies about the Local Group. An excess of bright satellites relative to model predictions was noted even in early semi-analytic models of the Local Group (e.g., Benson et al. 2002). More recently, numerical simulations indicated that galaxies like the MW should only very rarely host a pair of satellites as massive or bright as the Magellanic Clouds (Boylan-Kolchin et al. 2010; Busha et al. 2011; see also González et al. 2013). It has now been confirmed by several observational studies that the MW is indeed unusual in this respect (James & Ivory 2011; Liu et al. 2011; Robotham et al. 2012; although see also Tollerud et al. 2011). The two Magellanic Clouds are also on similar orbits and probably fell in together; they may have once formed a group including other MW satellites (Lynden-Bell & Lynden-Bell 1995; Nichols et al. 2011; Sales et al. 2011; Pawlowski & Kroupa 2013; Wang et al. 2013; Bozek et al. 2013). Very recently, a similar orbital grouping has been discovered around M31 (Ibata et al. 2013). In short, both of the two main Local Group satellite systems appear to have their idiosyncrasies. The models invoked to explain the abundance of satellite galaxies, however, usually assume the Local Group populations are typical, so this is an important assumption to verify.

Beyond average numbers, one might also wonder what, if any, is the relationship between the properties of the satellite population and the properties of the primary galaxy they orbit, e.g., its total stellar mass, morphology, or recent merger history. To address this issue it is important to find Local Group analogues, isolated bright galaxies with populations of dwarf satellites that are well-enough sampled to determine their clustering scale length, the amplitude of the satellite luminosity function, and the distribution of dwarf colors, morphology and other properties, information we have so far only for the Local Group dwarfs.

There has been much recent progress identifying satellites around normal galaxies. The easiest to study are bright companions like the Magellanic Clouds, M33 or M32, which are only 3–4 mag fainter than their primaries (e.g., Liu et al. 2011; Prescott et al. 2011; Sales et al. 2013; Guo et al. 2012; see Wang & White 2012 for earlier references). Fainter satellites have also been detected statistically using large-area ground-based surveys, as an excess of faint objects clustered around a population of brighter primary galaxies (Carlberg et al. 2009; Lares et al. 2011; Guo et al. 2011; Wang & White 2012; Jiang et al. 2012; Strigari & Wechsler 2012; Ruiz et al. 2013). Finally, space-based imaging has allowed these searches to be extended to higher redshift. In recent work, for instance, Nierenberg et al. (2011, 2012) have detected satellites extremely close to central galaxies, by selecting smooth early-type galaxies as primaries and subtracting from the image a model fit to their light.

So far, most of these studies have considered large but relatively distant samples of primaries, selected in all but a few cases from the Sloan Digital Sky Survey (SDSS; York et al. 2000). As a consequence, measurements of the satellite luminosity function have generally been limited to satellites 6–8 mag fainter than their primary (corresponding to r-band magnitudes $M_r = -14$ to -12). The missing satellite problem becomes most severe further down the luminosity function, however, so it is important to seek out fainter satellites in a large sample of nearby systems. In particular, searches for companions should target primary galaxies at distances intermediate between those of the few nearest groups (5 Mpc or less) and those typical of SDSS samples (200–400 Mpc or more, e.g., Lares et al. 2011; Guo et al. 2011; Strigari & Wechsler 2012; Ruiz et al. 2013).

In this paper, we search for excess clustering of SDSS galaxies around a sample of primary galaxies within 42 Mpc of us. At these very small distances, we can use size cuts to eliminate many of the more distant background galaxies, making the selection of local dwarf candidates relatively efficient, at the expense of completeness. The proximity of these galaxies also allows us to probe at least part of the satellite luminosity function 4–5 mag below most previous results.

The outline of the paper is as follows. In Section 2 we describe our primary and satellite samples; in Section 3 we measure the clustering signal and explore its dependence on primary luminosity and morphology, and in Section 4 we determine the relative luminosity function per primary. In Section 5 we summarize our results and discuss the prospects for future searches using data from deeper surveys.

2. THE SAMPLES

Our goal is to find faint satellites around systems roughly comparable to the primaries of the Local Group, and thus we want to search around nearby primaries with luminosities and/or stellar masses comparable to the MW and M31. Furthermore, the primary sample must overlap with a large-area survey such as the SDSS, and contain enough galaxies to obtain reasonable statistics. A recent catalog that satisfies these requirements is the parent catalog of the Atlas-3D survey (Cappellari et al. 2011). We discuss this primary sample, and our construction of a background/satellite sample, below.

2.1. Primaries

Our sample of primary galaxies is drawn from the Atlas3D parent catalog of Cappellari et al. (2011). The Atlas3D survey targeted nearby, bright early-type galaxies. These were selected from a larger parent sample of bright elliptical, S0, and spiral galaxies that was designed to be volume-limited above a certain stellar mass. The parent sample was constructed using K_s-band magnitudes from the Two Micron All Sky Survey (2MASS; Skrutskie et al. 2006), and the best distance estimates available from the literature. Given these distance estimates, the parent catalog is complete down to $M_{K_s} = -21.5$ out to a distance of 42 Mpc, corresponding to a stellar mass limit of $M_\star \geqslant 6 \times 10^9\ M_\odot$. It covers 37% of the sky, corresponding to a volume of 1.16×10^5 Mpc^3 out to 42 Mpc. The full catalog contains 871 galaxies, including 68 ellipticals, 192 S0s, and 611 spirals

Many of the galaxies in the parent sample are members of nearby galaxy clusters such as Virgo. In order to restrict our search to systems more analogous to the Local Group, we apply an isolation criterion to the parent sample. First, we remove M31 from the sample, since it is so nearby that its projected virial radius overlaps with many background systems. We then make a series of isolation and quality-control cuts on the sample:

1. We remove any member of the sample that is within a (3-D) distance of 1.5 Mpc of another member. This reduces the catalog to 356 galaxies, and excludes most cluster members.

2. We remove objects that are not in the SDSS footprint, or are in badly masked regions or regions of incomplete coverage. This reduces the sample to 282 galaxies.
3. We remove a further 5 galaxies which are within 5° of the center of the Virgo cluster in projection, and 3 galaxies which are within 3° of the center of the Coma or Leo clusters.

After making these cuts, we are left with 274 primaries, all isolated massive galaxies within 42 Mpc with good coverage in SDSS.

The Atlas3D catalog provides distances, morphological T-types, and (2MASS) K_s magnitudes for the sample. We also obtain total r-band magnitudes from SDSS where possible. In cases where the latter are poorly determined due to the large angular size or brightness of the galaxies, we estimate the total r magnitude from the RC3 B magnitude (de Vaucouleurs et al. 1991) using the color conversions and mean colors for different morphological types given in Fukugita et al. (1995), or we use the 2MASS K_s magnitude and assume the $r - K_s$ color is equal to the mean of the entire sample, $r - K_s = 2.9$. The dispersion in $r - K_s$ color for the sample is ± 0.9, so this gives an indication of the possible uncertainty in the final r magnitude for these systems (13/274 primaries, or 5% of the sample).

The primary K_s magnitudes range from -21.5 to -25.6. The average magnitude is $\langle M_K \rangle = -22.88$, and 95% of the sample are fainter than $M_K = -24.5$. Given that the absolute magnitude of the Sun in the K_s band is estimated to be $M_{K,\odot} = 3.29$ (Blanton & Roweis 2007), the primary luminosities range from 8.2×10^9 to $3.6 \times 10^{11} L_{K,\odot}$, with an average of $2.9 \times 10^{10} L_{K,\odot}$. Williams et al. (2009) derive a mean K_s-band mass-to-light ratio of $(M/L)_{K_s} = 1.09$ for a sample of 14 S and S0 galaxies, with a rms scatter of 30%. The appropriate value for ellipticals may be slightly higher (e.g., Bell et al. 2003), although it shows little systematic variation with color in the sample of Williams et al. (2009). We conclude that our primaries have a mean stellar mass of $\sim$3–3.5 $\times 10^{10} M_\odot$, with a range of $1 \times 10^{10} M_\odot$ to $4 \times 10^{11} M_\odot$, although 95% are below $1.5 \times 10^{11} M_\odot$. Using the mean stellar-to-halo-mass ratio determined by Leauthaud et al. (2012) from a combination of galaxy–galaxy lensing, clustering and abundance matching, this should correspond to an average halo mass of $1 \times 10^{12} M_\odot$, and a full range from $4 \times 10^{11} M_\odot$ to $1 \times 10^{14} M_\odot$ or more. The abundance matching model of Guo et al. (2010) also predicts similar values.

Abundance matching on the entire Atlas3D catalog, we would associate the 5% most luminous galaxies with halos in the mass range 10^{13}–$10^{14} M_\odot$ or more. These would correspond, however, to central galaxies in local groups and clusters such as Virgo. Our isolation criteria will remove these galaxies from the primary sample, and thus we expect our most luminous systems to occupy halos with masses of a few times $10^{13} M_\odot$ or less. The corresponding virial radii for our sample in a concordance Λ-CDM cosmology range from 200–600 kpc, or 0.°39–1.°15 at 29.7 Mpc, the mean distance to our primaries.

2.2. Satellites

Around our final sample of primaries, we search for potential satellites at projected separations up to 1 Mpc (corresponding to 2.°86 at a distance of 20 Mpc, or 1.°43 at 40 Mpc), in SDSS Data Release 8 (DR8; Aihara et al. 2011). In principle, we could apply a cut on photometric redshift to keep only those objects likely to be close to our primary sample, which extends out to $z \sim 0.01$. In practice, SDSS photometric redshifts have large uncertainties over the redshift and magnitude ranges of interest; after examining the photometric redshift estimates of objects at known distances, we choose to make a relatively conservative cut at $z_{\rm phot} = 0.15$. We use an SQL query of the SDSS Catalogue Archive Server[1] to retrieve any object that is within 1 Mpc projected separation from a primary galaxy and has a photometric redshift of 0.15 or less.

Regions of SDSS DR8 have been masked due to halos from bright stars or other artifacts. In order to obtain reliable background statistics, such as galaxy counts in circular annuli, it is necessary to identify the boundaries of masked regions and correct for the section of each annulus that has been cut out of the data. To detect masked regions automatically, we construct a square grid covering each field and search for cells devoid of catalog objects. The cell size is chosen so that each cell should contain 4 objects on average, in the case of a uniform distribution. Masked sections are identified as sets of two or more adjacent cells that contain no objects. Once a masked section is detected, any adjacent empty cells are added to it to find the total extent of the masked region.

For objects in the vicinity of each primary, we record magnitude and size. SDSS provides several measures of galaxies' apparent magnitudes. Of these, we use composite model (*cmodel*) magnitudes. These are calculated from exponential and de Vaucouleurs fits in each photometric band, using the linear combination of the two that best fits the image. Strauss et al. (2002) report that *cmodel* magnitudes are less dependent on local seeing variations than other measures, and are thus a good proxy to use as a universal magnitude for all types of objects. These magnitudes are extinction corrected; we do not K-correct them since the sample is local. For size, we use the exponential scale radii provided by SDSS to quantify galaxy size, since the light profiles of fainter dwarf galaxies are generally well-fit by exponentials (Mateo 1998).

In order to reduce the background of distant galaxies included in the satellite sample, the SDSS data are cut by magnitude, color, and size:

1. First, since the limiting r-band photometric magnitude in SDSS is about 22, galaxies that appear to be dimmer than this, or brighter than an apparent magnitude of $m_r = 10$, are eliminated as well.
2. Second, we apply a color cut, removing any objects with extreme colors and restricting our sample to galaxies with

$$-1 \leqslant (g - r) \leqslant 0.85\,.$$

   This corresponds broadly to the color range of local galaxies, allowing for large errors in color at faint magnitudes.
3. The most important cut on the data is a magnitude-dependent size cut. Only galaxies with exponential scale lengths $r_{\rm exp}$ and magnitudes m_r such that

$$24 < m_r - \frac{r_{\rm exp}}{1''} < 30 \qquad (1)$$

   are included in the sample, while larger and smaller objects are excluded. We discuss the logic and effectiveness of this cut in the Appendix. This cut has the effect of removing 98% of the remaining background, at the expense of reducing the satellite counts by an estimated 50%–70%, as discussed in the Appendix.

[1] CAS—http://skyservice.pha.jhu.edu/casjobs.

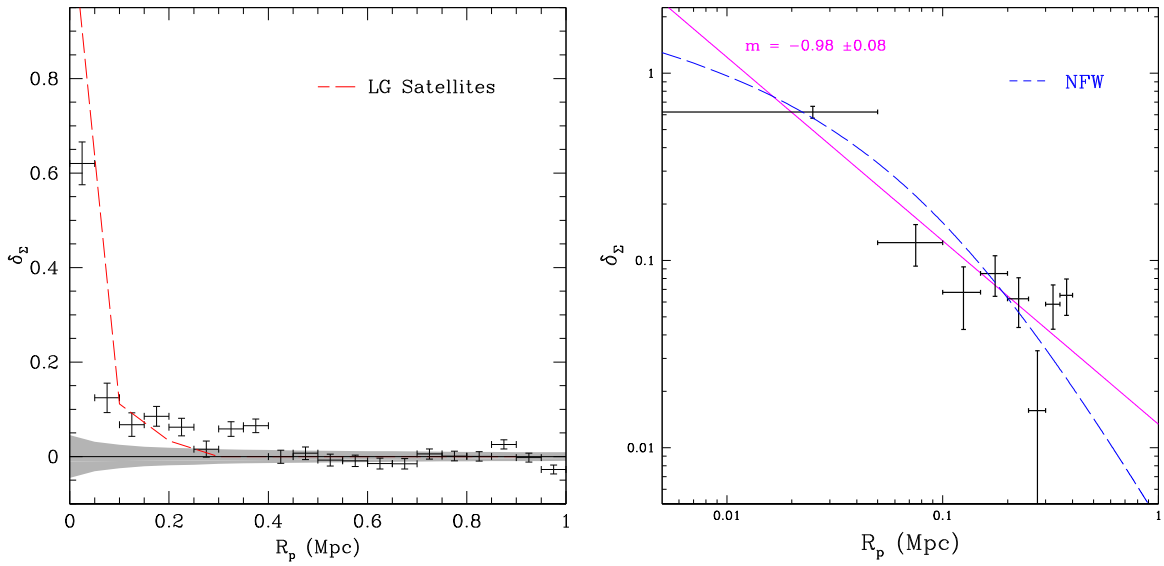

Figure 1. Left: the surface density contrast profile for the full sample. Gray shading indicates the rms scatter in the background surface density. The dashed line indicates the surface density of the Local Group comparison sample (see text), averaging over 3 projections. Horizontal error bars indicate bin widths, while vertical error bars indicate the uncertainty in δ_Σ, assuming Poisson errors in the galaxy counts. Right: the inner bins on a logarithmic scale, to highlight the radial dependence of the density excess. The solid line shows a linear fit to the inner bins of slope $m = -0.98$; the dashed curve shows a projected NFW profile of concentration $c = 10$.
(A color version of this figure is available in the online journal.)

3. THE CLUSTERING SIGNAL

We search for a satellite population by measuring the clustering of objects in the background catalog with respect to our primaries. Our method is similar to that in other recent studies (e.g., Liu et al. 2011; Lares et al. 2011; Guo et al. 2011). Possible systematics have been considered in detail by Chen et al. (2006) and Wang & White (2012).

3.1. Results for the Full Sample

After the background catalog is filtered using the cuts described above, we calculate projected separations R_p from the central primaries in linear units at the distance of the primary. Galaxies are binned by separation from the primary in bins of width 50 kpc, and the area on the sky in an annulus corresponding to each separation bin is calculated. We correct these areas for masking, as described above. In each bin, we calculate the surface density of galaxies Σ, and the density contrast relative to the background density $\overline{\Sigma}$, $\delta_\Sigma \equiv (\Sigma/\overline{\Sigma}) - 1$. We estimate the background density using a set of outer annuli with projected separations $R_p = 600$–950 kpc. The outermost annulus (950 kpc–1 Mpc) is excluded as it is subject to large masking corrections, while the inner limit of the background region is selected to minimize contamination from satellites, particularly in the most massive systems in our primary sample, which may have virial radii of 500–600 kpc. We discuss the effect of changing the inner limit of the background region briefly in sections 3.2 and 4.2 below. We also note that the innermost annulus ($R_p = 0$–50 kpc) may be contaminated by bright globular clusters or H II regions associated with the primary, and faint objects close to bright, extended ones can also have systematic errors in their SDSS photometry (Wang & White 2012); thus we will exclude this bin when calculating the cumulative excess within a given projected radius.

Figure 1 shows the surface density contrast as a function of projected separation. A positive contrast, corresponding to an overdensity of objects at projected separations $R_p \leqslant 400$ kpc, is detected at signal-to-noise ratio (S/N) ~ 9. The rms scatter in the background surface density is shown as the gray shading in the left-hand panel. We also plot the corresponding surface density contrast for a "Local Group comparison sample" (dashed red line in the left-hand panel). This consists of all the known members of the Local Group that would pass our cuts in size, magnitude, and color, if they were observed from a distance of 25 Mpc away. Numbers have been divided by two since there are two primaries in the Local Group.

We see the detected excess is comparable to that expected for a system like the Local Group, exceeding it slightly at large radii (200–400 kpc). (Some of the contribution from large radii may come from systems more massive than the MW or M31, as discussed in Section 3.2 below.)

In the right-hand panel of Figure 1, we plot the projected density contrast on a logarithmic scale, to emphasize the radial dependence. The mean logarithmic slope is $m \equiv d\ln\delta_\Sigma/d\ln r = -0.98 \pm 0.08$ (solid line), consistent with a projected isothermal profile ($m = -1$), but also with a projected Navarro–Frenk–White (NFW) profile (dashed blue curve). This is roughly as expected if satellites trace the mass of the halo surrounding each primary, although previous work indicates that the radial profile will depend on the details of the primary and satellite samples (Lorrimer et al. 1994; Chen et al. 2006; Chen 2008; Jackson et al. 2010; Sales et al. 2011; Lares et al. 2011; Tal et al. 2012; Nierenberg et al. 2011; Jiang et al. 2012; Wojtak & Mamon 2013; see Guo et al. 2012 and Nierenberg et al. 2012 for recent discussions).

The average excess satellite count per primary in the radial bin b, ΔN^b, is determined as

$$\Delta N^b = \frac{1}{N_{\rm gal}}\left(N^b_{\rm inner} - \frac{A^b_{\rm inner}}{A_{\rm outer}}N_{\rm outer}\right) \quad (2)$$

Where $N_{\rm gal}$ is the total number of primaries, $N^b_{\rm inner}$ is the number of galaxies in inner bin b, $A^b_{\rm inner}$ is the annulus area in bin b in the inner region, $A_{\rm outer}$ is the total area of the outer region, and $N_{\rm outer}$ is the number of galaxies in the outer region. The inner bins range from 50 to 600 kpc in projected radius around each

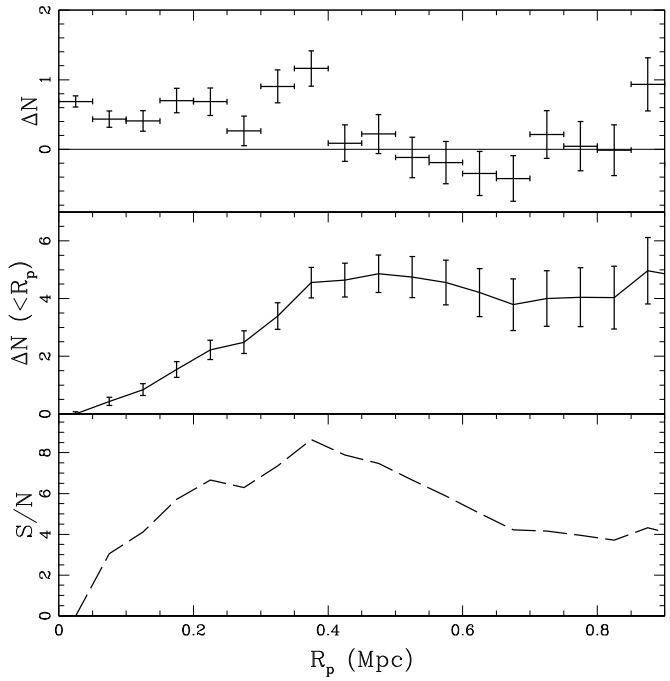

Figure 2. Average excess counts per galaxy ΔN in bins of projected radial separation R_p, for the full sample of 274 primaries. The top panel shows the excess counts in each bin, the middle panel shows the cumulative excess counts within a given projected separation, and the bottom panel shows the S/N of the cumulative excess.

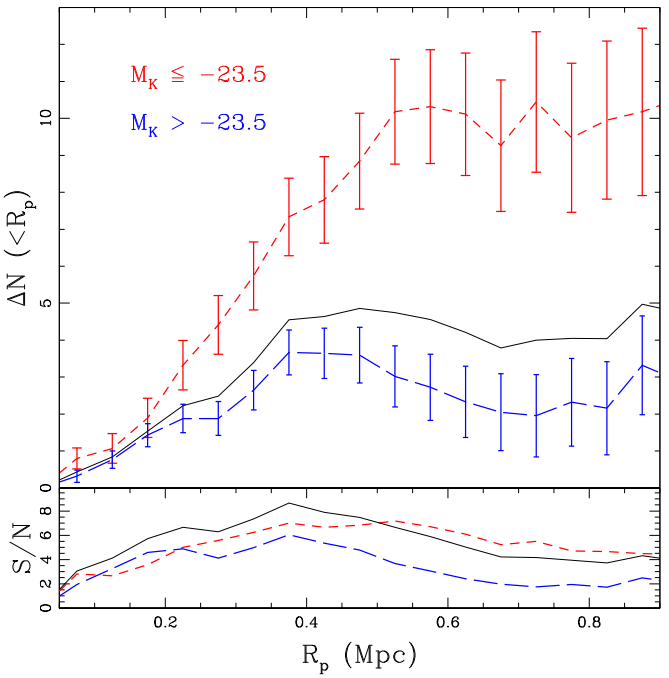

Figure 3. Cumulative excess counts per galaxy in bins of projected radial separation, as a function of primary magnitude. The top panel shows the cumulative excess, and the bottom panel shows the corresponding S/N. Red short-dashed lines indicate bright primaries ($M_K \leqslant -23.5$), blue long-dashed lines indicate faint primaries ($M_K > -23.5$), and black solid lines indicate the counts for the whole sample.

(A color version of this figure is available in the online journal.)

primary, while the outer region is the annulus ranging from 600 to 950 kpc in each case. The error in the final count per primary is calculated assuming Poisson errors on $N^b_{\rm inner}$ and $N_{\rm outer}$ and using the usual rules for error propagation; we ignore any contribution from uncertainties in the areas $A^b_{\rm inner}$ and $A_{\rm outer}$ which might arise from our masking corrections, as this is typically negligible.

The background correction $-(A^b_{\rm inner}/A_{\rm outer})N_{\rm outer}$ represents the mean surface density of the outer regions (R_p = 600–950 Kpc). Subtracting this term should remove both the contribution from uncorrelated galaxies and the contribution from large-scale ("two-halo") clustering, which dominates on scales of a few Mpc (e.g., Liu et al. 2011). There has been some discussion of whether using a locally determined background in clustering measurements introduces bias and/or reduces the S/N (Wang & White 2012). We have tested the effect of determining the values of $A_{\rm outer}$ and $N_{\rm outer}$ individually for each primary, or calculating an average background for all primaries first, and then scaling and subtracting this following Equation (2). We find that the clustering signal is very similar in both cases. The S/N is marginally higher using an average background (8.6 versus 7.2), so we have used this method in what follows.

Figure 2 shows the excess counts per bin (top panel), the cumulative excess within a given radius (middle panel), and the S/N of the cumulative detection (bottom panel). Errors on the cumulative counts are simply the errors on individual bins, added in quadrature. The S/N we define as the cumulative excess within some radius, divided by its error. In calculating the cumulative counts and S/N, we exclude the innermost bin (R_p = 0–50 kpc) to avoid contamination from the primary, as discussed previously. Integrating out to $R_p = 400$ kpc where we reach the best S/N, we find a net excess of 4.55 ± 0.53 satellites per central galaxy, at S/N = 8.6.

3.2. Dependence on Primary Luminosity

To test the dependence of the satellite population on primary luminosity, we split the full sample into two subsamples: 66 bright primaries with $M_K \leqslant -23.5$ and 208 fainter primaries with $M_K > -23.5$. The average K_s magnitudes for the two samples are −24.1 and −22.5, corresponding to luminosities of 9.3×10^{10} and 2.1×10^{10} $L_{\odot,K}$ respectively. The top panel of Figure 3 shows the cumulative number overdensity profiles for each subsample. Red (short-dashed) lines indicate the brightest primaries, blue (long-dashed) lines indicate fainter primaries, and black (solid) lines show the average for the whole sample. The bottom panel shows the S/N of each cumulative detection. As before, our error bars assume Poisson errors in the counts per bin. We find a strong dependence in the number of associated satellites on primary magnitude, with the brightest 25% of the sample having a cumulative count of associated satellites 3 times higher than the remaining 75% of the sample. The shape of the cumulative number profile also changes slightly with primary magnitude; in bright systems counts appear to rise out to projected separations of 500–600 kpc, whereas for the fainter primaries they reach a maximum by 400 kpc. Indeed, the relative difference between the bright and faint samples depends slightly on how we define our background region; after experimentation we have set the inner boundary to 600 kpc, as smaller values reduce the amplitude of the bright signal relative to faint signal, suggesting that the satellite populations of bright primaries extend out at least this far.

Overall, primaries with K_s-band magnitudes $M_{K_s} \leqslant -23.5$, shown in red, have the greatest signal of 10.2 ± 1.4 galaxies in excess of the background at an S/N of ∼7.3 in the 500–550 kpc projected radial separation bin. Primaries with $M_{K_s} > -23.5$

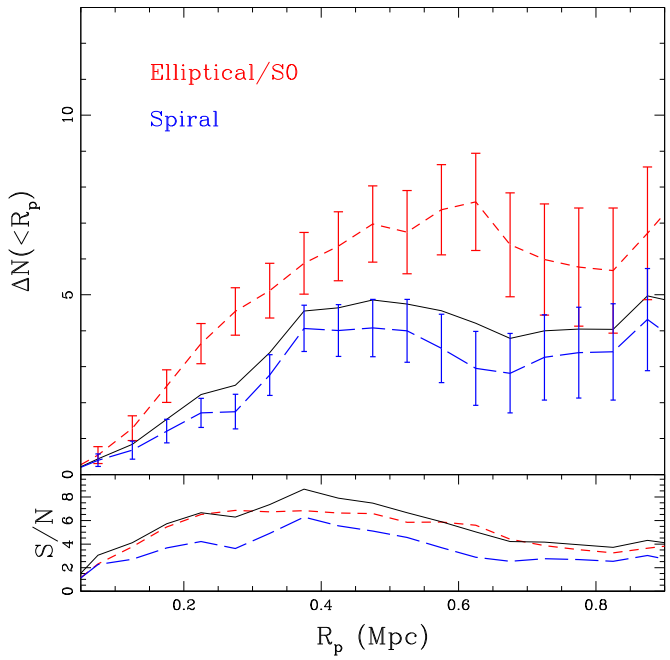

Figure 4. As Figure 3, but for primaries split by morphology. Red short-dashed lines indicate ellipticals and S0s ($T \leqslant 0$), blue long-dashed lines indicate spirals ($T > 0$), and black solid lines show the counts for the whole sample.

(A color version of this figure is available in the online journal.)

have 3.7 ± 0.6 satellites each within a projected radius of 350–400 kpc, where the S/N reaches a maximum of ∼6.

3.3. Dependence on Primary Morphology

We also split our primary sample by morphology into elliptical/S0 ($T \leqslant 0$; 73 in total) and spiral ($T > 0$; 201 in total) types, as determined by the Atlas3D survey (Cappellari et al. 2011). These two samples have almost identical mean magnitudes and rms scatter in the *K*-band ($M_K = -22.87 \pm 0.88$ and $M_K = -22.88 \pm 0.90$ respectively). As before, the cumulative excess counts for each case are shown in Figure 4. Elliptical primaries appear to have more satellites than spirals (7.6 ± 1.4, versus 4.1 ± 0.65), spread out over a slightly larger spatial scale (∼650 kpc versus 400 kpc, or a factor of 1.6). Although the contrast between the two subsamples is less marked than in the previous section, the difference in abundance and clustering scale suggests that they occupy halos of different mean mass. Although the S/N is low in our split samples, if we take the difference in clustering scale at face value it suggests a difference in halo mass of ∼4 ($= 1.6^3$) at *fixed K-band luminosity*. Thus, we find tentative evidence for morphological dependence in the ratio of near-infrared luminosity to dark matter halo mass. This could indicate differences in the mass-to-light ratios of the stellar populations, which may account for as much as a factor of ∼2 (e.g., Bell et al. 2003), or a more fundamental difference in the stellar-to-halo-mass ratio (SHMR; e.g., Leauthaud et al. 2012). Previous estimates of halo mass have already suggested a difference in the SHMR of this order between the most massive early and late-type galaxies (e.g., Wojtak & Mamon 2013, and references therein). The difference seen here is only of marginal (2.5σ) significance, however, and it could also be that a few massive systems are biasing our subsample of ellipticals and S0s. With an all-sky sample or deeper imaging around our current sample, we should be able to test for morphological dependence more convincingly.

3.4. Dependence on Satellite Color

Finally, we can attempt to determine how the clustering signal varies with satellite color. We might expect red and blue satellites to cluster on different scales, given the morphology-density relation observed in the Local Group (e.g., McConnachie 2012). In large samples, the clustering amplitude of brighter satellites also depends on secondary as well as primary color (e.g., Wang & White 2012). Testing color cuts on our background sample, however, we find that most (∼85%) of the clustering signal comes from blue ($g - r \leqslant 0.6$) satellites. (As discussed in Section 5, approximately 75% of Local Group galaxies are this blue.) This may be partly due to our size cut, blue galaxies being larger at fixed luminosity. As it is, the clustering signal for blue satellites is similar to the signal for the whole sample, while the S/N for red satellites alone is too low to detect any obvious differences in clustering strength for this population.

4. THE RELATIVE LUMINOSITY FUNCTION

Our final goal is to construct a relative luminosity function for our satellite population, which is the mean number of satellites per primary with magnitudes in some range relative to the primary, $N(\Delta m)$ where $\Delta m = m_{\rm sat} - m_{\rm main}$. This function, considered previously by many other groups (e.g., Liu et al. 2011; Lares et al. 2011; Guo et al. 2011, 2012; Nierenberg et al. 2011; Strigari & Wechsler 2012; see Nierenberg et al. 2012 for a summary) provides an interesting point of comparison to the relative mass function $N(M_{\rm sat}/M_{\rm main})$ often studied in CDM simulations. In order to compare directly with the previous results we calculate the magnitude difference in the SDSS *r*-band, using primary *r* magnitudes estimated as discussed in Section 2.1.

The MW is the obvious point of comparison for relative luminosity functions, and most previous authors have defined subsamples of their data thought to match its properties, in particular its luminosity in the *r*-band. The luminosity usually assumed corresponds to a total magnitude of $M_{r,\rm MW} \sim -21$, based on the *V*-band magnitude estimate from van den Bergh (2000) (e.g., Liu et al. 2011). This is comparable to the mean *r* magnitude of our bright ($M_K \leqslant -23.5$) sample, $\langle M_r \rangle = -21$. The mean halo mass of the bright sample, when estimated as described in Section 2.1, is probably 3–4 $\times$ $10^{12}\,M_\odot$, however—that is twice the estimated mass of the MW's halo. Furthermore, our bright sample also includes at least a few systems with much larger halo masses of a few times $10^{13}\,M_\odot$. Thus, the MW may be intermediate between the average properties of our bright and faint subsamples. To provide a reasonable point of comparison, we define an intermediate sample in the *r*-band, of the 132 primaries with $M_r = -21 \pm 1$. This intermediate sample has a $L_K = 5 \times 10^{10}\,L_\odot$, suggesting a mean halo mass of 1.5–2 $\times$ $10^{12}\,M_\odot$, closer to the estimates of the MW's halo mass. The sample has a mean distance of 31 Mpc.

Figure 5 shows the excess counts for the "MW-like" sample with $M_r = -21 \pm 1$ (solid black line with error bars), compared with our full sample (dotted black line), and the K_s-band bright and faint subsamples (red and blue short and long-dashed lines respectively). The counts are intermediate between the bright and faint samples, and increase out to at least 500 kpc. Overall, the largest S/N of ∼6 occurs at $R_p \sim 400$ kpc, where we find an excess of 4.9 ± 0.8 galaxies above the background, (although the S/N remains similar out to 600 kpc, where the excess is 6.7 ± 1.2 galaxies). For the calculation of the relative luminosity function we will include counts between projected radii of

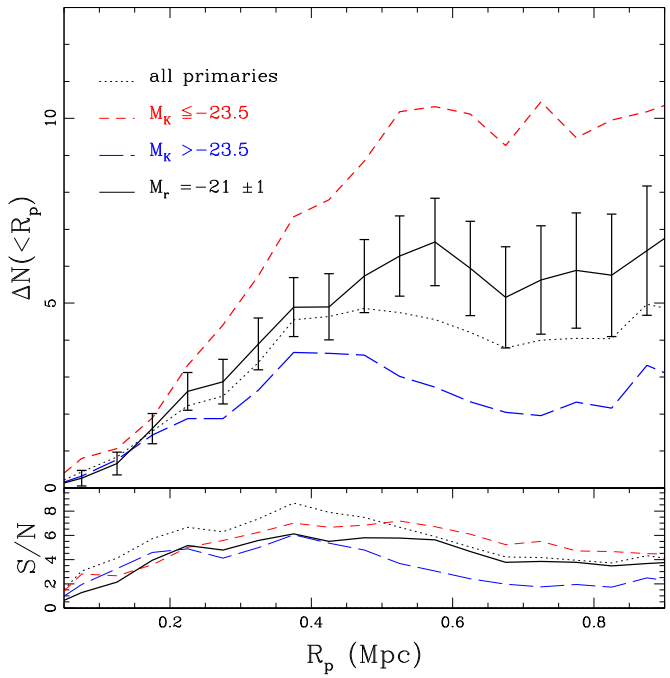

Figure 5. Top: cumulative excess counts per galaxy in bins of radial separation, for primaries with $M_r = -21 \pm 1$ (magenta solid lines with error bars), compared with the bright subsample (short-dashed red lines), the faint subsample (long-dashed blue lines), and the entire sample (dotted black lines). Bottom: the corresponding S/Ns.

(A color version of this figure is available in the online journal.)

50 and 400 kpc, to maximize the S/N for the MW-like sample while avoiding possible contamination from the primary.

4.1. Optimal Weighting

Splitting the satellite sample into many Δm_r magnitude bins greatly reduces the S/N per bin, particularly for smaller subsamples of the primaries. Due to the drastic reduction in number counts per bin, we run into the problem of extremely noisy background estimates. To overcome this we use a mean background model to determine the relative excess in counts.

First, we construct an apparent (r-band) luminosity function for all the SDSS galaxies in the satellite sample, as defined in Section 2.2. For a given primary of magnitude $m_{r,\mathrm{main}}$, we then calculate the fraction of the satellite sample which would lie within a relative magnitude offset Δm_r of $m_{r,\mathrm{main}}$. Finally we multiply this fraction by the *total* background counts around the primary. This gives us a smoother estimate of the average background expected in a single Δm_r bin.

The S/N in a given bin can still vary strongly from one primary to the next, particularly since our primary galaxies are at different distances, and thus the magnitude limit of the survey will exclude different Δm_r bins for different primaries. To produce an optimal estimate of the mean luminosity function, we calculate the average satellite count in each bin using inverse-variance weighting for the contributions from individual primaries. Thus the average count in bin i, $\overline{n}_i$ is calculated using

$$\overline{n}_i = \frac{\sum_{j=1}^{n} \left(n_{i,j}/\sigma_{i,j}^2\right)}{\sum_{j=1}^{n} \left(1/\sigma_{i,j}^2\right)}, \quad (3)$$

where $n_{i,j}$ is the unweighted count for primary j in bin i, and $\sigma_{i,j}^2$ is the uncertainty in the counts for that primary and bin.

4.2. Comparison to the Milky Way and to Previous Work

Figure 6 shows the cumulative relative luminosity function in r-band magnitude, $N(\Delta m_r)$, for our bright ($M_K \leqslant -23.5$) and faint ($M_K > -23.5$) subsamples (left-hand panel blue and red points respectively). Only satellites between projected radii of 50 and 400 kpc are included. The errors bars are the uncertainty in the inverse-variance weighted average. As discussed previously, the MW may be intermediate between these two samples; the right-hand panel shows the average luminosity function for the MW-like sample with $M_r = -21 \pm 1$ (points with error bars). The solid blue line shows the relative luminosity function for known MW satellites, with cuts in size, magnitude, color and projected radius applied as if they were seen at 31 Mpc, the mean distance to our MW-like sample of primaries. The dashed red and dotted magenta lines show the relative luminosity function for MW satellites with only a magnitude cut, or with no cuts at all, respectively.

The relative luminosity function has been measured previously around more distant samples of primaries, down to $\Delta m_r \sim 8$. Nierenberg et al. (2011) measured down to $\Delta m_r = 6$ around GOODS ellipticals at redshifts 0.1–0.8, for instance; Lares et al. (2011) measured to $\Delta m_r = 7$–8 in SDSS for galaxies at $z = 0.03$–0.1 (i.e., distances of 120–400 Mpc); Guo et al. (2011) made similar measurements over a wider range of primary luminosity and out to z = 0.5; Strigari & Wechsler (2012) measured down to $\Delta m_r = 8$, but also obtained upper limits on the satellite abundance down to $\Delta m = 10$. These results are summarized in Nierenberg et al. (2012), who also show measurements down to $\Delta m_r = 8$ from COSMOS HST images (see also work since by Wang & White 2012; Jiang et al. 2012). A number of studies have also considered separately the abundance of brighter, LMC-like satellites with Δm =3–5 (e.g., Liu et al. 2011; Prescott et al. 2011; Sales et al. 2013; Guo et al. 2012). Below $\Delta m = 8$, the only discoveries outside the Local Group have been serendipitous (e.g., James & Ivory 2011, who identified four individual satellites below $\Delta m = 8$ using narrow-band $H\alpha$ imaging, but were only complete to $\Delta m \sim 5$). Thus, our result extends most previous measurements of satellite abundance by 4–5 mag further down the luminosity function.

Previous work reached several general conclusions on the relative luminosity function, as reviewed in Nierenberg et al. (2012). Satellite counts are reasonably well fit by a Schechter function, with a shallow power-law slope at intermediate magnitudes (e.g., Lares et al. 2011 measure $\alpha = 1.3 \pm 0.2$), which may steepen at the faint end, below $\Delta m = 5$–6. On average the slope is steeper than those measured for satellites of the MW or M31, with slightly fewer bright satellites above $\Delta m = 6$, and more satellites below this. The normalization depends strongly on primary luminosity, particularly at the bright end where the number of satellites with $\Delta m < 5$ varies by factors of several, e.g., between a sample with $\log M_{*,\mathrm{main}} = 10.5$–11 and a sample with $\log M_{*,\mathrm{main}} = 11$–11.5 (Nierenberg et al. 2012, Figure 7; see also Nierenberg et al. 2013 where the luminosity dependence is studied in detail). The variations in slope and normalization at the faint end are less clear. There is a weaker dependence on primary color or morphology, with red primaries having more satellites at a given Δm. There appears to be little or no dependence on the redshift of the sample, at least out to $z \lesssim 1$.

Our results are roughly consistent with these trends, though with some interesting differences. We find less variation in normalization between our bright and faint samples, possibly because they are both at the faint end of the range studied in

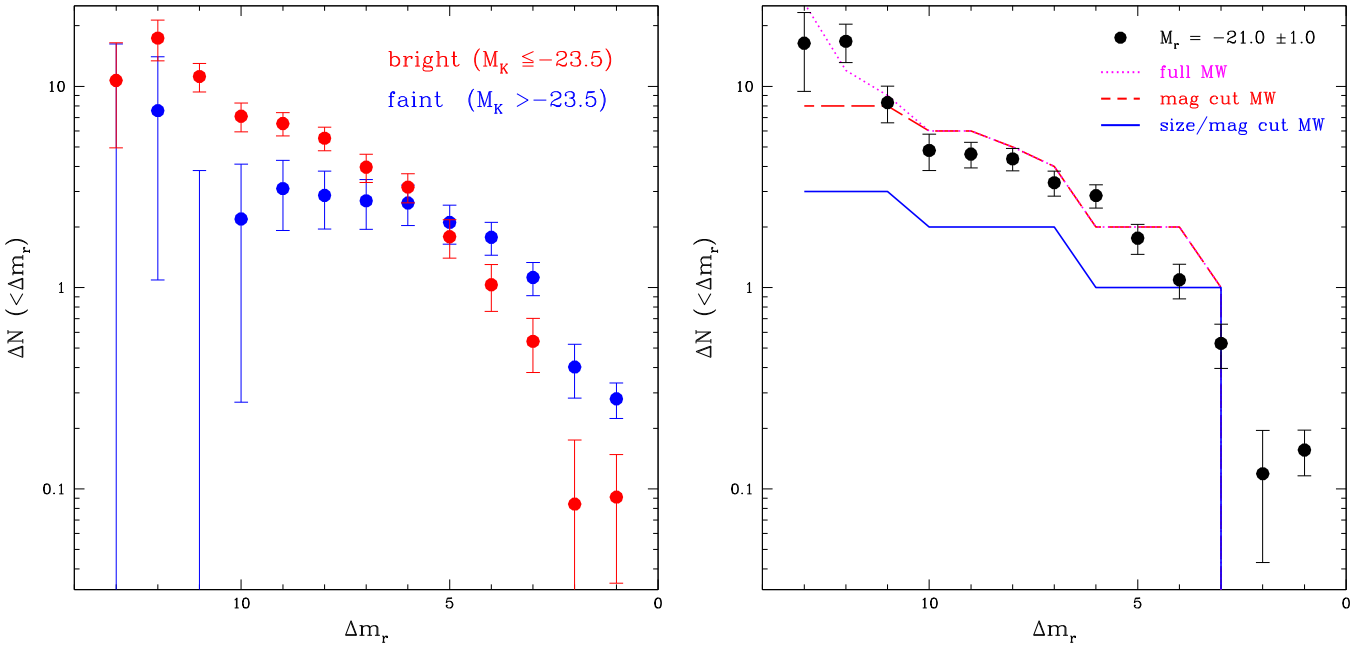

Figure 6. Left: the cumulative relative luminosity function $N(<\Delta m_r)$, which is the mean number of satellites per primary, with r-band magnitudes Δm or less being fainter than the primary, as a function of Δm. Red indicates bright primaries; blue indicates faint primaries. Averages and error bars are calculated using simulated background counts and inverse-variance weighting, as described in the text. Right: the same for a "MW-like" sample with $M_r = -21 \pm 1$, compared with the relative luminosity function for the MW, with size and magnitude cuts (solid blue line), a magnitude cut only (dashed red line), or no cuts on size or magnitude (dotted magenta line).

(A color version of this figure is available in the online journal.)

previous work. Our isolation cuts may also bias our bright sample to lower mean halo masses than purely magnitude-selected samples. Our MW-like sample is similar to the lowest luminosity bin of Guo et al. (2011), however, and for it we find results consistent with theirs over the range $\Delta m = 1$–6 (see their Figure 7). For our bright sample, the cumulative counts rise roughly as a power law below $\Delta m = 6$, as seen in Nierenberg et al. (2012). The faint end rise is steeper than seen for the satellites of the MW, once our cuts in size, magnitude, and color are taken into account (solid blue curve in the right-hand panel). The MW also has an excess of bright, Magellanic-Cloud-like systems with $\Delta m < 6$, although this is only significant for the LMC itself after our cuts are taken into account. Intriguingly, however, we find that fainter primaries have a flatter relative luminosity function, and more satellites with $\Delta m \leqslant 4$. This suggests that satellites like the Magellanic Clouds might be somewhat less exceptional if the luminosity and/or mass of the MW had been *overestimated*. We note recent work by González et al. (2013) shows that less massive halos are also more likely to host a close pair of subhalos with separations and velocity differences as small as those of the Magellanic Clouds.

We note however several caveats when comparing our measured luminosity function to that of the MW. First, our cuts in size and magnitude, required to eliminate the large number of background galaxies, will also exclude the most compact dwarfs. We have also cut out the innermost annulus ($R_p = 0$–50 kpc) to remove contamination from bright globular clusters and H II regions, as distinguishing these from satellites in a systematic way would require detailed photometric and/or morphological analysis. In the case of the MW, this could remove several nearby satellites from our sample, depending on the projection considered. Comparing the three curves in the right-hand panel of Figure 6, we conclude that our final counts may be incomplete by a factor of two to three due to the size, magnitude, color and projected separation cuts. Accounting for this incompleteness, the relative luminosity function of the MW satellites lies a few objects below our average counts in the range $\Delta m = 5$–10. On the other hand, the census of MW satellites may still be incomplete as well, particularly around $\Delta m \sim 10$, due to extinction in the plane of the disk. Our mean value may also be slightly affected by systematics; reducing the inner boundary of the background region to 500 kpc, for instance, reduces the amplitude of the relative luminosity function by 20%–30%. Overall, our results provide a measurement of the average abundance of a subset of the satellites around galaxies like the MW down to $\Delta m \sim 12$–13, that is $M_r = -9$ to -8, as well as a lower bound on the total abundance of all satellites in this magnitude range.

Figure 7 compares our derived relative luminosity function to the "low mass, low redshift" samples from Nierenberg et al. (2012) (open triangles and squares indicate early and late types respectively, offset slightly in Δm_r for clarity), and to the measurements and upper limits from Strigari & Wechsler (2012) (solid red pentagons and arrows), as well as to the relative luminosity function of the MW (with line styles as in Figure 6). All three studies are in reasonable agreement for $\Delta m_r \sim 1$–6, and highlight the unusual brightness of the Magellanic Clouds (i.e., the high MW counts at $\Delta m_r = 3$–5). Around $\Delta m_r = 5$, our results are somewhat higher than those of other groups, although statistically consistent at the 1–2σ level. We note systematics may be relevant here; in particular reducing the inner limit of our background region from 600 to 500 kpc shifts these points down by $\sim 1\,\sigma$. It is possible that our MW-like sample includes a few massive systems with extended satellite distributions that increase the relative luminosity function by 20%–30% at these magnitudes, relative to the samples of Nierenberg et al. (2012) and Strigari & Wechsler (2012).

For $\Delta m_r \sim 6$–8, our results flatten, suggesting incompleteness may become significant here. Applying our size, magnitude and projected radius cuts to the satellites of MW, we expect to be

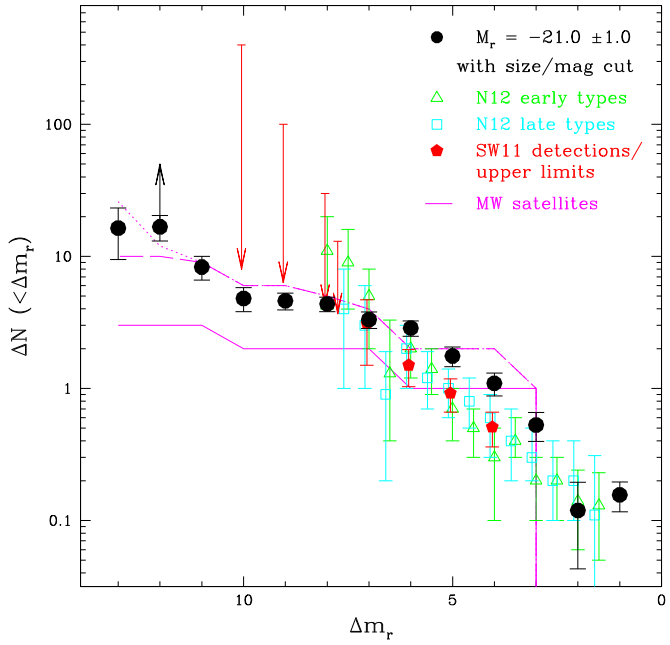

Figure 7. Relative luminosity function for the "MW-like" sample (solid black circles), compared to previous measurements by Nierenberg et al. (2012) (open triangles and squares) and measurements and upper limits from Strigari & Wechsler (2012) (solid red pentagons and arrows). At fainter magnitudes, we expect our results to be incomplete by a factor of 2–3 due to our morphological selection, as indicated by the upward arrow at $\Delta m_r = 12$. Magenta lines show the relative luminosity function of the MW for comparison, with line styles as in Figure 6.

(A color version of this figure is available in the online journal.)

incomplete by a factor of at least 2–3 at faint magnitudes, as indicated by the different MW samples. The upward arrow on the data point at $\Delta m_r = 12$ illustrates the effect of correcting for this incompleteness. With this correction, our results are in good agreement with those of Nierenberg et al. (2012) at $\Delta m_r = 7$–8, and provide a lower bound to the results of Strigari & Wechsler (2012) below this.

4.3. Spectroscopic Confirmation

Clustering on the sky gives only statistical evidence for association between faint and bright galaxies. It is natural to want to confirm this for individual objects, using redshifts. Given the magnitude range and spatial distribution of our satellites, this will be logistically challenging. We can obtain redshifts for a small number of the brightest satellites from SDSS itself, however. The limiting r-band magnitude of the SDSS spectroscopic catalog is 4.5 mag brighter than that of the photometric catalog, so we will only be able to detect the satellite population down to $\Delta m \sim 7$–8, but we can nonetheless use these bright objects to check for consistency with our clustering results.

Selecting all galaxies with spectra within $R_p = 1$ Mpc of our primaries, and applying the same cuts in size, magnitude and color to the spectroscopic catalog as we have the photometric catalog, we find a total of 7732 objects at all redshifts around 244 of our primaries. Using primary redshifts from SDSS or the NASA/IPAC Extragalactic Database,[2] we calculate the velocity offset $\Delta V = V_{\rm sat} - V_{\rm main}$. The left panel of Figure 8 shows the distribution of ΔV versus R_p, for the 1159 objects with $|\Delta V| < 1200$ km s^{-1}. An overdensity of points is clearly visible at $|\Delta V| < 200$ km s^{-1}, corresponding roughly to the velocity dispersion of our primary halos. (We note that the area sampled increases linearly with R_p, explaining why there is also a horizontal gradient in density across the plot.) Not all the objects with small ΔV are satellites, however; this can be inferred from the fact that the overdensity extends all the way out to 1 Mpc projected separation. In fact, this overdensity at large radii and small ΔV corresponds to the "two-halo term" in galaxy clustering. The characteristic spatial scale of the two-halo term for our primaries is roughly 4 Mpc, which translates into a redshift range of ± 300 km s^{-1}.

Some fraction of the objects with small velocity offsets are genuine satellites. We can see this by combining clustering measurements in both position and velocity space. The right-hand panel of Figure 8 shows the distribution of velocity offset for objects within three different radial ranges, 0–400, 0–200, and 0–100 kpc respectively from top to bottom (solid lines). The dotted line shows the distribution of velocity offset for $R_p = 0.5$–1 Mpc, rescaled to the three other distributions so that they agree at large ΔV. The inner radial bins show a clear excess of objects at $\Delta V \lesssim 200$ km s^{-1} relative to the distribution at large projected radii. The excess corresponds to ~100 satellites within 100 or 200 kpc projected, or 0.4 satellites per primary galaxy. Our photometric results indicate we should have 1–2 satellites within these radii, down to $\Delta m \sim 12$; given the shape of the relative luminosity function we expect the numbers at $\Delta m = 7$–8 to be reduced by a factor of 3–4 relative to those at $\Delta m = 12$, so the abundance of spectroscopic satellites seems consistent with the clustering measured from the photometric catalog. This provides an additional consistency check of our previous results and a rough limit on our incompleteness, down to $\Delta m_r \sim 8$.

Overall, the distribution of velocity offsets shown in the right-hand panel of Figure 8 can be understood as the sum of a two-halo term which follows the dotted line, and a one-halo term responsible for the excess at small radii. This illustrates a practical complication in confirming the association of satellites with primaries. Since the spatial extent of the two-halo term along the line of sight translates into a velocity offset comparable to the expected velocity dispersions of our primary halos, separating the one- and two-halo components requires some caution. Even at relatively small projected separation ($R_p < 100$ kpc), the two-halo term still contributes 15%–25% of the excess counts at $\Delta V \leqslant 200$ km s^{-1}.

5. SUMMARY AND FUTURE PROSPECTS

The faint satellites of bright galaxies such as the MW and M31 provide an important test of galaxy formation models within the CDM framework. Unfortunately, few other samples of faint dwarfs exist comparable to those available in the Local Group. Several groups have made progress on this problem recently, identifying the brighter satellites of large numbers of isolated luminous galaxies. Using a very local sample of bright galaxies, we have extended this work 4–5 mag down the luminosity function, to satellites 12–13 mag fainter than their primaries. Although the sample is incomplete, it gives us a partial estimate of the satellite luminosity function down to the bottom of the "classical" dwarf range, $M_r \sim -8$, and rules out a large population of faint dwarfs over a range of sizes and magnitudes corresponding to ~30% of the Local Group population.

We have shown in particular that it is possible to detect very nearby satellites using relatively shallow photometry. The key to

[2] NED—http://ned.ipac.caltech.edu

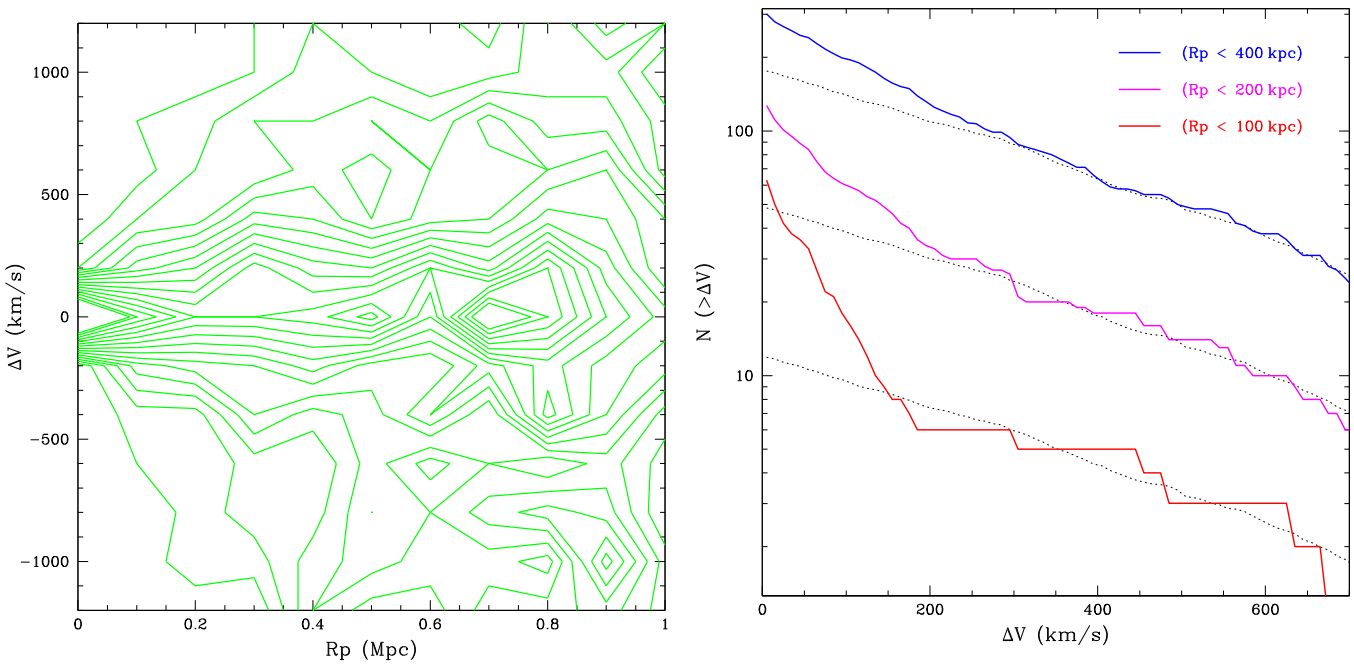

Figure 8. Left: velocity offset from the primary ΔV vs. projected separation R_p, for the (brightest) satellites with spectroscopic redshifts. Contours show the number of satellites in intervals of 2/200 km s^{-1}/0.1 Mpc. Right: number of objects with velocity offsets less than ΔV, in radial ranges R_p = 0–100 kpc (lower red curve), 0–200 kpc (middle magenta curve), or 0–400 kpc (upper blue curve). The dotted line shows the distribution of ΔV at large radii (0.5–1 Mpc), normalized to match each distribution at large values of ΔV.

(A color version of this figure is available in the online journal.)

reducing background contamination is a magnitude-dependent size cut, which for very nearby systems selects out relatively low-surface-brightness dwarfs. For nearby, faint galaxies, this is more effective than selection using SDSS photometric redshifts, which can have errors of ±0.05 (±200 Mpc) or more. The result is a strong detection of a clustering signal, corresponding to a large population of satellites per primary. We note however that the satellite population detected is incomplete by construction, excluding the most and least compact objects. Given our cuts, we find 4.55 ± 0.53 satellites per primary in our full sample (4.9 ± 0.8 for our MW-like sample) at projected separations R_p = 50–400 kpc. Although we lack the S/N to measure an accurate radial profile, the projected distribution is consistent with an isothermal or NFW profile, extending out to ∼400 kpc.

Splitting our primary sample by luminosity, the 25% brightest primaries ($M_{K_s} \leqslant -23.5$) have ∼3 times more satellites than the fainter primaries, in a distribution extending out to 500–600 kpc. Abundance matching and weak gravitational lensing suggest the mean halo mass of our whole primary sample is $\sim 1 \times 10^{12}\, M_\odot$, and the mean virial radius should be 250 kpc (though some dynamical studies of satellites give a slightly higher mass estimate; cf. More et al. 2011, as discussed in Leauthaud et al. 2012). The bright subsample should occupy halos 3–4 times more massive than those of the fainter primaries, with a virial radius of ∼400 kpc, although our isolation criteria may bias the mean mass of the sample slightly. Given these mass estimates, our satellite detections extend out to 1–1.5 virial radii in projection, and satellite abundance varies approximately linearly with halo mass. The former result is consistent with expectations from simulations; the linear dependence of abundance on halo mass is probably an accidental consequence of the halo mass range sampled. Over a larger range the relationship between stellar and halo mass ratio changes slope, affecting satellite abundance (e.g., Sales et al. 2011).

Splitting the sample by morphology, the ellipticals appear to have 85% ± 35% more satellites than spirals, clustered on a larger spatial scale of 500–600 kpc, even though the average luminosities of the two subsamples of primaries are equal. Thus, we find evidence for a morphological dependence of the stellar luminosity to halo mass ratio, albeit at marginal statistical significance. This could reflect differences in the mass-to-light ratio of the stellar populations, or possibly a more fundamental difference in the stellar-to-halo mass ratio (SHMR).

Our color distribution is slightly bluer than that of the Local Group, with only 15% of objects having $(g - r) > 0.6$ ($\sim(B - V) > 0.8$, Fukugita et al. (1995)). In the Local Group approximately 25% of satellites are known to be this red, although global color measurements are incomplete and highly uncertain, particularly at faint magnitudes (Mateo 1998). Guo et al. (2011) found similar results, but only for brighter satellites ($\Delta m \leqslant 6$). In subsequent work (Guo et al. 2012) they also showed that red satellites cluster more strongly than blue satellites, so it may be that a larger fraction of red satellites are excluded by our inner radial cut at 50 kpc. Our size cut may also have an effect on the color distribution; in particular, decreasing the lower bound on $r_{\rm exp}$ might reveal more of the faint red dwarf spheroidals common in the Local Group. Nonetheless, understanding the color dependence of the abundance and spatial distribution of satellites remains problematic, as discussed in the most recent work by Guo et al. (2013).

Beyond this statistical detection of the satellite population, confirming the identity of individual satellites will be challenging. While satellites could in principle be identified spectroscopically, the field sizes and magnitude limits make this prohibitively expensive for a large sample of primaries. Furthermore, because the two-halo clustering scale maps onto a line-of-sight velocity range comparable to the internal velocity dispersion of a bright galaxy halo, separating satellites from

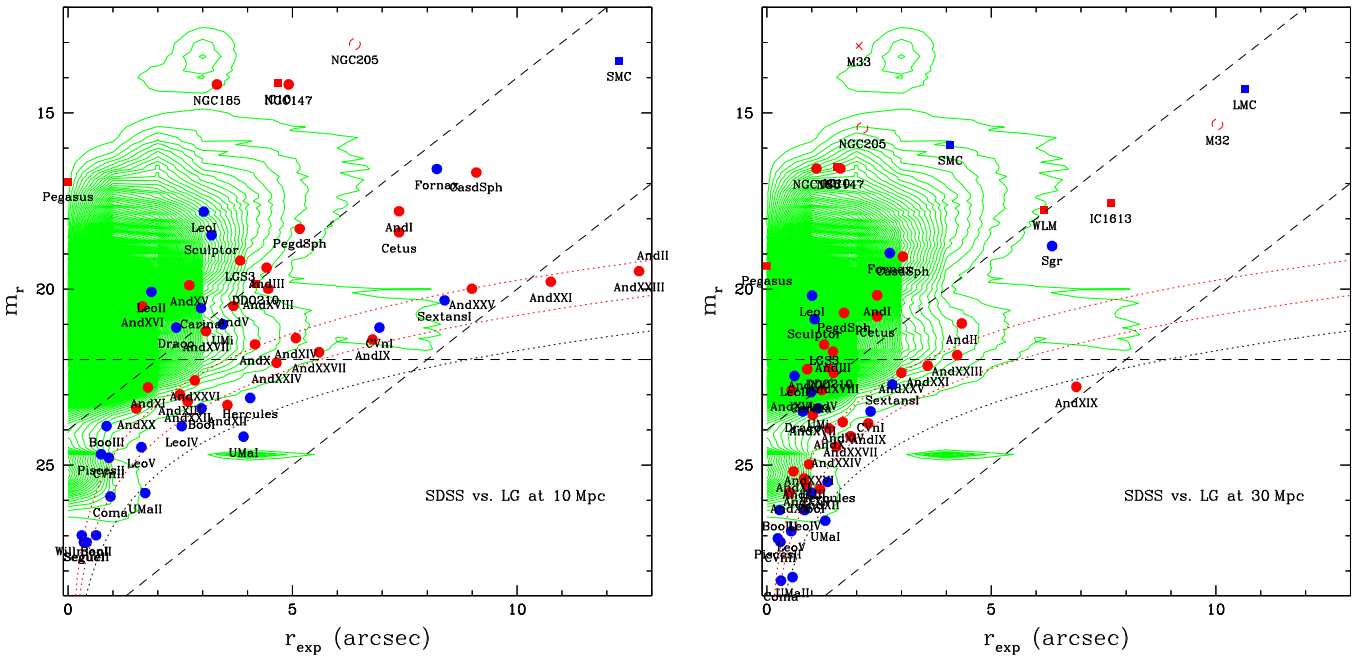

Figure 9. Distribution of SDSS galaxies in apparent r-band magnitude m_r vs. exponential scale radius r_{exp} (green contours). The left- and right-hand panels show the LG comparison sample as it would appear at distances of 10 and 30 Mpc, respectively. Dotted curves indicate the region where SDSS becomes incomplete due to surface brightness limits. Dashed lines indicate the cuts applied to the satellite sample.

(A color version of this figure is available in the online journal.)

interlopers is not completely trivial even with full velocity information, as discussed in the preceding section.

It would be easy, however, to obtain deeper photometry on many or all of our target fields. These extend our 1–2 deg around each primary, and are well-suited to large-area cameras such as MegaCam (Boulade et al. 2003) or Hyper Suprime-Cam (Takada 2010). Surveys with these instruments could extend the clustering measurement around a nearby sample like the Atlas3D sample down to larger Δm, or they could compile better statistics on a larger sample of primaries 2–3 times further away. The only uncertainty in making projections for such follow-up work is to determine the efficiency of the size cut for different distance ranges and magnitude limits. Larger samples would be invaluable, however, to clarify the detailed radial distribution, anisotropy, and color distribution of faint satellites, the importance of halo-to-halo variations, and the link between faint satellites and primary properties. One intriguing idea is to use faint satellite counts as a proxy for halo mass, since simulations suggest the two should correlate reasonably well over certain ranges of primary and satellite luminosity (e.g., Nickerson et al. 2013). While the potential accuracy of this method is unclear, it might just be possible to test it directly at slightly larger distances than those considered here by combining clustering measurements with optimally weighted galaxy–galaxy lensing.

Larger samples of faint satellites would provide useful input to models of galaxy formation as well. A particularly important goal, as discussed in the introduction, is to understand what produces the cutoff in the efficiency of galaxy formation. If galaxy formation is stochastic on small scales, for instance, as suggested both by spatial clustering (Taylor et al. 2004; Kravtsov et al. 2004), and by rotation curves or velocity dispersion profiles (Boylan-Kolchin et al. 2011), what is the hidden variable, if any, that determines which subhalos form stars? The Local Group doesn't have enough faint objects to distinguish easily between alternate models, and may not be representative in any case, so finding well-sampled Local Group analogues is essential in the longer term.

We thank Jonathan Grossauer, Gretchen Harris, Michael Balogh, Anna Nierenberg, Tommaso Treu, Michael Drinkwater, Simon Driver, Aaron Robotham, Anne-Marie Weijmans, and the participants of the KITP Workshop "First Galaxies and Faint Dwarfs," for helpful discussions. We also wish to thank the anonymous referee for a number of suggestions to improve the paper, and the Atlas3D and SDSS teams for making their catalogs available to the community. This work was supported by a Discovery Grant to JET from the Natural Sciences and Engineering Research Council (NSERC) of Canada.

This project has made use of data from the Sloan Digital Sky Survey III (SDSS-III). Funding for SDSS-III has been provided by the Alfred P. Sloan Foundation, the Participating Institutions, the National Science Foundation, and the U.S. Department of Energy Office of Science. SDSS-III is managed by the Astrophysical Research Consortium for the Participating Institutions of the SDSS-III Collaboration—see the SDSS-III Web site http://www.sdss3.org for a full list of institutions.

APPENDIX

MORPHOLOGICAL SELECTION

Galaxies in SDSS have a particular distribution of sizes as a function of magnitude, reflecting their intrinsic physical properties and redshift distribution. While we don't know what dwarf satellites around nearby luminous galaxies would look like a priori, we can estimate this by taking the known members of the Local Group (LG) and placing them at the same range of distances as our primaries. Figure 9 shows this comparison, placing LG galaxies at distances of 10 Mpc (left-hand panel) and 30 Mpc (right-hand panel). The green contours show the distribution of SDSS galaxies from the (inner and outer) regions

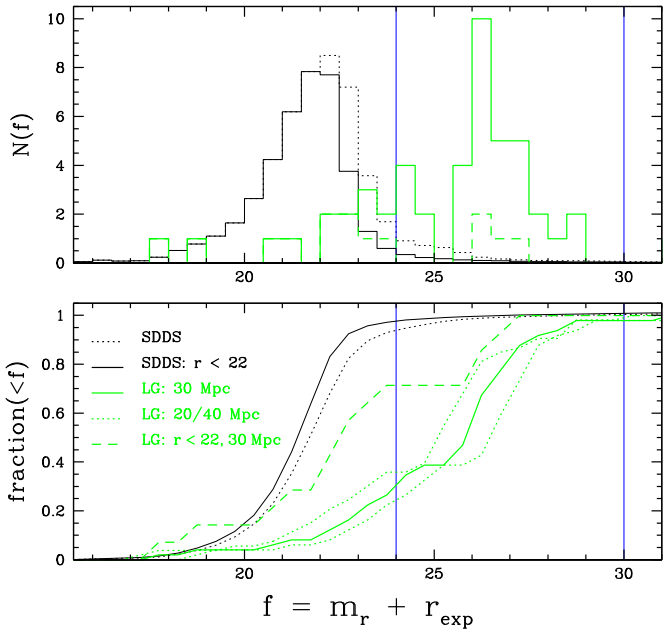

Figure 10. Top: normalized distributions of f values for the SDSS sample with and without a cut at $m_r = 22$ (solid and dotted black histograms) and the LG comparison sample (solid and dashed green histograms). Horizontal lines show our size–magnitude cuts at $f = 24$ and $f = 26$. Bottom: the corresponding cumulative distributions. The LG comparison sample is shown at distances of 30 Mpc (solid green lines) and 20/40 Mpc (dotted green lines) without a magnitude cut, as well as at 30 Mpc with a magnitude cut (dashed green line).

(A color version of this figure is available in the online journal.)

around our primary sample. The symbols show the satellites of the MW (blue) and Andromeda (red).

The SDSS photometric catalogs become increasingly incomplete below $r \sim 22.5$ (York et al. 2000; Aihara et al. 2011), so we place a cut at $r = 22$ (horizontal dashed line) to avoid photometric incompleteness. The SDSS surface brightness limit is more complicated, depending on the size, magnitude and morphology of the object. SDSS catalogs start to become significantly incomplete at central surface brightnesses of $\mu_0 \simeq 24$–24.5 (Blanton et al. 2005), although some objects can be recovered down to $\mu_0 \simeq 26$–26.5 (Kniazev et al. 2004). The dotted curves on Figure 9 correspond to $\mu_0 = 24.5, 25.5$ (red) and 26.5 (black), assuming an exponential light profile.

In the region of parameter space where SDSS is complete, we see that our LG comparison sample generally lies to the right of the main SDSS distribution, that is to say nearby analogues of LG dwarfs would be larger than typical background galaxies at a given magnitude. If we select objects to the right of a diagonal running across the plot, we expect to eliminate most of the background galaxies, while retaining at least some of the nearby dwarfs. Thus, we define a function $f = m_r + r_{\rm exp}$, and cut out galaxies with $f < 24$ (leftmost diagonal lines on Figure 9). This leaves us with a region of parameter space still partly affected by surface brightness incompleteness; to reduce the impact of this effect while retaining some faint, extended objects, and to have well-defined limits for our sample, we place an upper cut at $f = 30$ (rightmost diagonal lines on Figure 9). Thus the region above the horizontal and between the diagonal dashed lines on Figure 9 represents our selection box for potential dwarfs. Note that this region contains only a fraction of the LG comparison sample; the exact fraction will depend on the distance to the primary.

The top panel of Figure 10 shows the normalized distributions of f values for the SDSS sample with and without a cut at $m_r = 22$ (solid and dotted black histograms) and the LG comparison sample (solid and dashed green histograms). We see a clear offset between the values, motivating our choice of cuts. The bottom panel shows the corresponding cumulative distributions. Placing a cut at $f = 24$ (vertical blue line) eliminates 98% of the SDSS galaxies brighter than $m_r = 22$, reducing the background in our clustering measurements. Unfortunately, the cuts also eliminate a significant fraction of the LG comparison sample—the cut at $f = 24$ is expected to eliminate 25%–35% of the sample, depending on distance (lower solid and dotted green curves), while the cut in magnitude eliminates a further

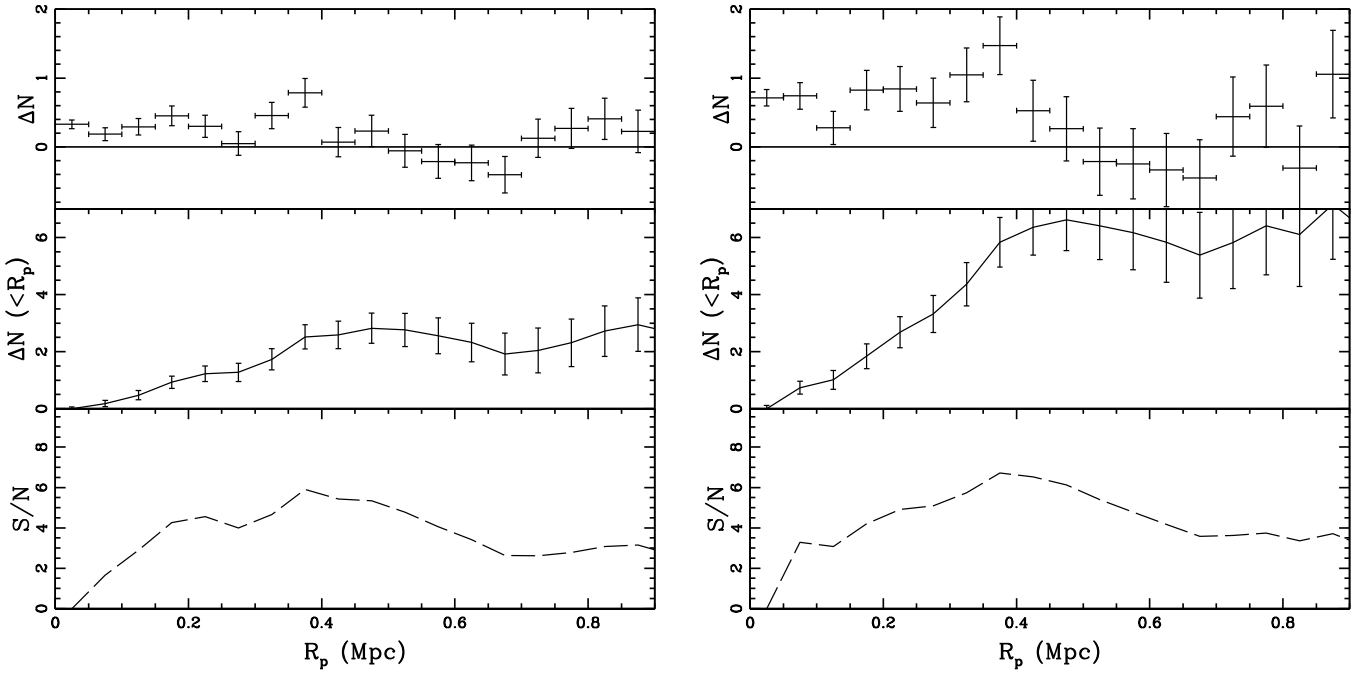

Figure 11. As Figure 2, but for size–magnitude cuts $24 < f < 26$ (left panel) and $23 < f < 30$ (right panel).

40%. Thus the anticipated completeness in the satellite sample is ∼30%.

While our cuts are motivated by the distributions of parameters shown above, we can test their effectiveness by varying the limiting values of f and measuring the clustering signal. Figure 11 shows the differential and cumulative excess counts, as well as the S/N, as in Figure 2, but using the cuts $24 < f < 26$ (left panel) and $23 < f < 30$ (right panel). In both cases, we detect a signal similar to that seen in Figure 2, but at lower significance (S/N ∼ 6–6.7). We have tested the effect of varying the upper and lower cuts in f, as well as the cut in r magnitude, and confirmed that our choice of $24 < f < 30$, $m_r < 22$ is close to optimal, given our primary sample and the properties of DR8.

Clearly, it is disappointing to have to eliminate 2/3 of all potential satellites from our secondary sample. This is required, however, in order to reduce the background, which otherwise would dominate the counts by a factor of 600 or more. In comparing our detected satellite populations to that of the MW, we must keep this incompleteness in mind and apply the same cuts to the MW population. Future surveys with lower magnitude and surface brightness limits should help improve this situation. Finally, we note that the cuts used here are not necessarily optimal: we could make cuts that depend on primary distance, for instance, or on the color or photometric redshift of the secondary. All of these possibilities would probably improve the S/N of our detection, at the expense of a more complicated selection function.

REFERENCES

Aihara, H., Allende Prieto, C., An, D., et al. 2011, ApJS, 193, 29
Barkana, R., & Loeb, A. 1999, ApJ, 523, 54
Behroozi, P. S., Wechsler, R. H., & Conroy, C. 2013, ApJ, 770, 57
Bell, E. F., McIntosh, D. H., Katz, N., & Weinberg, M. D. 2003, ApJS, 149, 289
Belokurov, V., Zucker, D. B., Evans, N. W., et al. 2006, ApJL, 647, L111
Benson, A. J., Bower, R. G., Frenk, C. S., et al. 2003, ApJ, 599, 38
Benson, A. J., Frenk, C. S., Lacey, C. G., Baugh, C. M., & Cole, S. 2002, MNRAS, 333, 177
Blanton, M. R., Lupton, R. H., Schlegel, D. J., et al. 2005, ApJ, 631, 208
Blanton, M. R., & Roweis, S. 2007, AJ, 133, 734
Boulade, O., Charlot, X., Abbon, P., et al. 2003, Proc. SPIE, 4841, 72
Boylan-Kolchin, M., Bullock, J. S., & Kaplinghat, M. 2011, MNRAS, 415, L40
Boylan-Kolchin, M., Springel, V., White, S. D. M., & Jenkins, A. 2010, MNRAS, 406, 896
Bozek, B., Wyse, R. F. G., & Gilmore, G. 2013, ApJ, 772, 109
Bullock, J. S., Kravtsov, A. V., & Weinberg, D. H. 2000, ApJ, 539, 517
Busha, M. T., Wechsler, R. H., Behroozi, P. S., et al. 2011, ApJ, 743, 117
Cappellari, M., Emsellem, E., Krajnović, D., et al. 2011, MNRAS, 413, 813
Carlberg, R. G., Sullivan, M., & Le Borgne, D. 2009, ApJ, 694, 1131
Chen, J. 2008, A&A, 484, 347
Chen, J., Kravtsov, A. V., Prada, F., et al. 2006, ApJ, 647, 86
Dekel, A., & Silk, J. 1986, ApJ, 303, 39
de Vaucouleurs, G., de Vaucouleurs, A., Corwin, H. G., Jr., et al. 1991, Third Reference Catalogue of Bright Galaxies (New York: Springer)
Efstathiou, G. 1992, MNRAS, 256, 43P
Fukugita, M., Shimasaku, K., & Ichikawa, T. 1995, PASP, 107, 945
Gnedin, N. Y., & Kravtsov, A. V. 2006, ApJ, 645, 1054
González, R. E., Kravtsov, A. V., & Gnedin, N. Y. 2013, ApJ, 770, 96
Governato, F., Brook, C., Mayer, L., et al. 2010, Natur, 463, 203
Gunn, J. E., & Gott, J. R., III 1972, ApJ, 176, 1
Guo, Q., Cole, S., Eke, V., & Frenk, C. 2011, MNRAS, 417, 370
Guo, Q., Cole, S., Eke, V., & Frenk, C. 2012, MNRAS, 427, 428
Guo, Q., Cole, S., Eke, V., Frenk, C., & Helly, J. 2013, MNRAS, 434, 1838
Guo, Q., White, S., Li, C., & Boylan-Kolchin, M. 2010, MNRAS, 404, 1111
Ibata, R. A., Lewis, G. F., Conn, A. R., et al. 2013, Natur, 493, 62
Jackson, N., Bryan, S. E., Mao, S., & Li, C. 2010, MNRAS, 403, 826
James, P. A., & Ivory, C. F. 2011, MNRAS, 411, 495
Jiang, C. Y., Jing, Y. P., & Li, C. 2012, ApJ, 760, 16
Karachentsev, I. D. 2005, AJ, 129, 178
Kauffmann, G., White, S. D. M., & Guiderdoni, B. 1993, MNRAS, 264, 201
Klypin, A., Kravtsov, A. V., Valenzuela, O., & Prada, F. 1999, ApJ, 522, 82
Kniazev, A. Y., Grebel, E. K., Pustilnik, S. A., et al. 2004, AJ, 127, 704
Koposov, S., Belokurov, V., Evans, N. W., et al. 2008, ApJ, 686, 279
Kravtsov, A. V., Gnedin, O. Y., & Klypin, A. A. 2004, ApJ, 609, 482
Lares, M., Lambas, D. G., & Domínguez, M. J. 2011, AJ, 142, 13
Leauthaud, A., Tinker, J., Bundy, K., et al. 2012, ApJ, 744, 159
Liu, L., Gerke, B. F., Wechsler, R. H., Behroozi, P. S., & Busha, M. T. 2011, ApJ, 733, 62
Łokas, E. L., Kazantzidis, S., & Mayer, L. 2012, ApJL, 751, L15
Lorrimer, S. J., Frenk, C. S., Smith, R. M., White, S. D. M., & Zaritsky, D. 1994, MNRAS, 269, 696
Lynden-Bell, D., & Lynden-Bell, R. M. 1995, MNRAS, 275, 429
Mashchenko, S., Wadsley, J., & Couchman, H. M. P. 2008, Sci, 319, 174
Mateo, M. L. 1998, ARA&A, 36, 435
Mayer, L., Mastropietro, C., Wadsley, J., Stadel, J., & Moore, B. 2006, MNRAS, 369, 1021
McConnachie, A. W. 2012, AJ, 144, 4
Moore, B., Ghigna, S., Governato, F., et al. 1999, ApJL, 524, L19
Moore, B., Katz, N., Lake, G., Dressler, A., & Oemler, A. 1996, Natur, 379, 613
More, S., van den Bosch, F. C., Cacciato, M., et al. 2011, MNRAS, 410, 210
Nichols, M., & Bland-Hawthorn, J. 2011, ApJ, 732, 17
Nichols, M., Colless, J., Colless, M., & Bland-Hawthorn, J. 2011, ApJ, 742, 110
Nickerson, S., Stinson, G., Couchman, H. M. P., Bailin, J., & Wadsley, J. 2013, MNRAS, 429, 452
Nierenberg, A. M., Auger, M. W., Treu, T., Marshall, P. J., & Fassnacht, C. D. 2011, ApJ, 731, 44
Nierenberg, A. M., Auger, M. W., Treu, T., et al. 2012, ApJ, 752, 99
Nierenberg, A. M., Oldenburg, D., & Treu, T. 2013, MNRAS, 436, 2120
Pawlowski, M. S., & Kroupa, P. 2013, MNRAS, 435, 2116
Prescott, M., Baldry, I. K., James, P. A., et al. 2011, MNRAS, 417, 1374
Rees, M. J., & Ostriker, J. P. 1977, MNRAS, 179, 541
Robotham, A. S. G., Baldry, I. K., Bland-Hawthorn, J., et al. 2012, MNRAS, 424, 1448
Ruiz, P., Trujillo, I., & Mármol-Queraltó, E. 2013, arXiv:1312.4533
Sales, L. V., Navarro, J. F., Cooper, A. P., et al. 2011, MNRAS, 418, 648
Sales, L. V., Wang, W., White, S. D. M., & Navarro, J. F. 2013, MNRAS, 428, 573
Silk, J. 1977, ApJ, 211, 638
Skrutskie, M. F., Cutri, R. M., Stiening, R., et al. 2006, AJ, 131, 1163
Strauss, M. A., Weinberg, D. H., Lupton, R. H., et al. 2002, AJ, 124, 1810
Strigari, L. E., & Wechsler, R. H. 2012, ApJ, 749, 75
Takada, M. 2010, in AIP Conf. Ser. 1279, Deciphering the Ancient Universe with Gamma-Ray Bursts, ed. N. Kawai & S. Nagataki (Melville, NY: AIP), 120
Tal, T., Wake, D. A., & van Dokkum, P. G. 2012, ApJL, 751, L5
Taylor, J. E., & Babul, A. 2001, ApJ, 559, 716
Taylor, J. E., Babul, A., & Silk, J. 2004, in ASP Conf. Ser. 327, Satellites and Tidal Streams, ed. F. Prada, D. Martinez Delgado, & T. J. Mahoney (San Francisco, CA: ASP), 205
Tollerud, E. J., Boylan-Kolchin, M., Barton, E. J., Bullock, J. S., & Trinh, C. Q. 2011, ApJ, 738, 102
Tollerud, E. J., Bullock, J. S., Strigari, L. E., & Willman, B. 2008, ApJ, 688, 277
van den Bergh, S. 2000, The Galaxies of the Local Group (Cambridge: Cambridge University Press)
Wang, J., Frenk, C. S., & Cooper, A. P. 2013, MNRAS, 429, 1502
Wang, W., & White, S. D. M. 2012, MNRAS, 424, 2574
White, S. D. M., & Frenk, C. S. 1991, ApJ, 379, 52
White, S. D. M., & Rees, M. J. 1978, MNRAS, 183, 341
Williams, M. J., Bureau, M., & Cappellari, M. 2009, MNRAS, 400, 1665
Willman, B., Dalcanton, J. J., Martinez-Delgado, D., et al. 2005, ApJL, 626, L85
Wojtak, R., & Mamon, G. A. 2013, MNRAS, 428, 2407
York, D. G., Adelman, J., Anderson, J. E., Jr., et al. 2000, AJ, 120, 1579
Zucker, D. B., Belokurov, V., Evans, N. W., et al. 2006, ApJL, 650, L41